An Adiabatic Foehn Mechanism

Florentin Damiens, François Lott, Christophe Millet, Riwal Plougonven

An Adiabatic Foehn Mechanism

Florentin Damiens[a], Francois Lott[a], Christophe Millet[b], and Riwal Plougonven[c]

[a]LMD Ecole Normale Supérieure, 75231 Paris, France
[b]CEA DAM DIF, 91297 Arpajon, France
[c]LMD Ecole Polytechnique, 91128 Palaiseau, France

Received* 14 June 2017; Accepted: 14 February 2018

Keywords: Foehn, mountain meteorology, mesoscale dynamics, gravity waves, critical level

Abstract

Atmospheric mountain flows produced when the incoming wind is small near the surface and continuously increases with altitude are evaluated with models of increasing complexity. All models confirm that foehn can be produced by a mountain gravity wave critical level mechanism, where the critical level is located below the surface. This mechanism does not involve humidity, upper level wave breaking, upstream blocking, downward wave reflections or hydraulic control as often suggested by popular theories. The first model used is a theoretical model which combines linear gravity wave dynamics with a nonlinear boundary condition: in this model the wave breaking does not feedback onto the dynamics by construction. Partial linear waves reflection are also minimized by using smooth profiles of the incident wind and a uniform stratification $N^2 = \text{cte}$, and can even be suppressed when the incident wind shear is also constant, $U_z = \text{cst}$. The second model is a numerical mesoscale model (Weather Research and Forecast), and we show that it predicts mountain wave fields that can be reproduced by the theoretical model, provided that we specify an adequate boundary layer depth in the theoretical model.

1 Introduction

Foehn flows are characterized by downslope winds that are warm, dry and strong and that generally occur on the lee side of mountains [Richner and Hachler(2013),]. For more than a century

*Quarterly Journal of the Royal Meteorological Society

they have been studied worldwide (see for three different mountain ranges [Brinkmann(1974), McGowan *et al.*(2002), Drobinski and Coauthors(2007)]), because they have strong economical impacts, for instance through increase in fire danger [Takane and Kusaka(2011), Sharples *et al.*(2010), Cannon *et al.*(2017),]), pollution [Seibert *et al.*(2000),] or weather hazards. They can also actively contribute to the climate change through their local impacts on sea ice melting [Elvidge *et al.*(2015),].

One long-standing question about foehn concerns the origin of the warming of the air masses, and it is generally admitted that there are two dominant mechanisms that can explain it [Richner and Hachler(2013),]. The first mechanism is along the line of meteorological textbooks [Seibert(2005),] when the example of the foehn is used to illustrate the significance of moist processes by using thermodynamical diagrams. In this "diabatic" theory, the warming of the air masses results from the forced condensation that occurs upstream of the ridge, the large temperature and dry air result from the flow descent on the lee side. As observational evidence suggests that warming has a more adiabatic cause [Seibert(1990),], a second mechanism, named "isentropic drawdown" is often proposed. In this mechanism, the foehn air comes from warmer and dryer altitudes upwind of the mountain because there is low level flow blocking. These two types of foehn, one diabatic with strong upstream ascent and one adiabatic with upstream flow blocking are sometimes referred to as Swiss and Austrian foehn respectively [Wursch and Sprenger(2015),]. With the progress of Lagrangian analysis, the relative amplitude of these two mechanisms is now better established [Smith *et al.*(2003), Miltenberger *et al.*(2016),] and it seems that the adiabatic mechanism is often more efficient that the diabatic one. The Lagrangian analyses also reveal that other irreversible processes can play a role, like the vertical mixing occurring when the air passes the mountain summit, and the radiative impact of the upstream clouds [Elvidge and Renfrew(2016),].

The fact that dynamics play such a central role in the foehn motivates the present paper. Actually, behind the apparently simple idea that upstream blocking elevates the air parcels before they abruptly descent on the lee side are hidden quite subtle nonlinear processes. These processes are controlled by the non dimensional mountain height, $H_N = \frac{HN}{U_\infty}$, where H is the maximum mountain height, N the buoyancy frequency and U_∞ a scale for the incident wind. When H_N is large, the vertical wavelength of the mountain waves U_∞/N is small compared to the mountain height H, the mountain waves break near above the mountain top, and the resulting nonlinear dynamics produce strong downslope winds and foehn (see the review by [Durran(1990)] and recent simulations in [Smith and Skyllingstad(2011)]). The mixing produced by the breaking waves can induce a well mixed stagnant layer, which allows to establish a correspondence with the fully nonlinear hydraulic jump theory ([Baines (1998), Smith(1985)]). The presence of the stagnant layer also permits to argue that nonlinear reflections at the self-induced critical level present in the mixed layer can reflect downward the waves and amplify the response [Laprise and Peltier(1989), Smith and Skyllingstad(2011),]. Also, for large H_N, part of the low level flow is blocked upstream making upstream blocking concomitant to the onset of foehn. All these efforts to interpret dynamically the onset of foehn in terms of breaking waves or blocking, hide the simple fact that some foehn can be produced by [Long(1953)]'s model for hydrostatic linear waves forced by a nonlinear boundary condition [Lilly and Klemp(1979), Muraki(2011),]. Interestingly, using such a model, [Lilly and Klemp(1979)] predict that the wave response is enhanced for mountains with a small windward and large leeward slopes, which is a form of "isentropic drawdown" mechanism produced by blocking, if we assume that the blocked air can be represented dynamically by a gentle

windward slope. Nevertheless, the results using [Long(1953)]'s type models are not much used to interpret foehn, essentially because when they produce foehn, they also predict intense wave breaking aloft which undermines all the linear interpretations of what occur downstream of the breaking zone (e.g which includes the foehn zone). As we shall see, low level wind shears can mitigate this upper level wave breaking because the mountain waves become less and less unstable with altitude when the wind increases.

Concerned with the recurrent problem in mountain meteorology theory that the near surface winds are ill defined ([Vergeiner(1971), Lott(2007)]) and can become very small, [Lott(2016)] (hereinafter L16) adapts the model of [Long(1953)] to incident shear flow that are null in $z = 0$. L16 shows that this induces a critical level dynamics near below the surface that produces downslope windstorm and foehn without upper level wave breaking. L16 also shows that downslope winds and foehn are favored when the surface flow is stable, i.e. when the surface Richardson number $J = N^2/U_z^2$ is large compared to its critical value, $J = 0.25$. As the model is linear, it also suggests that there is no need to interpret the onset of foehn in terms of upstream blocking, nonlinear internal wave reflections, or using hydraulic theory, which are all the ingredients that are often mentioned to explain adiabatic foehn.

The results in L16 have several limitations. The first is that the model in L16 is only adapted to situations when the shear layer depth, d, is much larger than the maximum mountain height, H, i.e. as long as the near critical level solutions in [Booker and Bretherton(1967)] can be used to treat the critical level. The second is that L16 does not explain why the results found are so sensitive to J. The third is that it does not exclude the possibility that reflections can play a role on foehn, because linear reflections can be present. The fourth is that the inflow equations used in [Long(1953)] are only rigorously valid when the incident flow is uniform. The last is the representation of boundary layer absorptive effects: L16 uses Raighleigh drag and Newtownian cooling with a free slip boundary condition. Some earlier studies have explored more realistic boundary conditions, e.g. for turbulent flow over hills [Hunt *et al.*(1988a), Hunt *et al.*(1988b),], or with viscous solutions [Lott(2007)]. In L16, these simplifications are made to ease the numerical treatment of the problem. They are in part justified by the fact that in the atmosphere the low level wind shears are often due to horizontal gradients in temperature, they do not solely result from boundary layer dynamics: they can extend well above it, and there the inviscid dynamics can be applied.

The purpose of the present paper is to fill these gaps by extending the L16's theory to taller mountains, and by validating it against fully nonlinear simulations. For this purpose, section 2 reformulates the results in L16 for a mountain of arbitrary height (not only for $H << d$) but still for small dissipation (when the linear drags correspond to a boundary layer depth $z_b << d$). Section 3 exposes the dry foehn mechanism proposed and shows that it is entirely related to the near-surface critical level dynamics. Section 4 presents fully nonlinear simulations done with WRF and explains how the value of z_b is chosen to enable a comparison of the theory with the numerical simulations. Section 5 characterizes systematically the results in terms of foehn intensity, downslope winds amplitude, and gravity wave stress. To check if the results remain robust beyond our simplified treatment of the boundary layer, it also presents tests where (i) the incident wind is not null at the surface and (ii) where a conventional atmospheric boundary layer scheme is used. Section 6 concludes and discusses further the relations with observations.

2 Theoretical model

To analyze the mountain waves produced by a stably stratified shear flow when the incident wind is null at $z = 0$, L16 considers the background flow profiles

$$U(z) = U_\infty \tanh(z/d), N^2(z) = \text{const}, \tag{1}$$

incident on a 2-dimensional mountain, the height of which follows the Witch of Agnesi profile

$$h(x) = \frac{H}{1 + \frac{x^2}{2L^2}}. \tag{2}$$

In (1), $U(z)$ is the background horizontal wind, $N(z)$ the Brunt Vaisala frequency, z the altitude, d is the vertical scale of the shear and U_∞ the incident wind maximum amplitude. In (2) H is the maximum mountain height, L its characteristic horizontal length, and x the horizontal coordinate. When scaling time by N^{-1} and distances by U_∞/N the 2-dimensional non-rotating linear dynamics can be expressed in term of a non dimensional vertical velocity, $\overline{w}(\overline{x}, \overline{z})$ of the form,

$$\overline{w}(\overline{x}, \overline{z}) = \int_{-\infty}^{+\infty} f(\overline{k}) \hat{w}_c(\overline{k}, \overline{z}) e^{i\overline{k}\overline{x}} d\overline{k}, \tag{3}$$

where overbars denote dimensionless variables, and $\hat{w}_c(k, z)$ is a canonical monochromatic solution of "unit" amplitude in the far field which satisfies the dissipative Taylor Goldstein equation,

$$\frac{d^2\hat{w}_c}{d\overline{z}^2} + \left[\frac{1}{\left(\overline{U} - i\frac{\overline{z}_k}{\sqrt{J}}\right)^2} - \frac{\overline{U}_{\overline{z}\overline{z}}}{\overline{U} - i\frac{\overline{z}_k}{\sqrt{J}}} - \overline{k}^2 \right] \hat{w}_c = 0. \tag{4}$$

In (3) the amplitude term $f(\overline{k})$ is obtained by numerical inversion of the non-linear free-slip boundary condition:

$$\overline{w}(\overline{x}, \overline{h}(x)) = \left(\overline{U}(\overline{h}) + \overline{u}(\overline{x}, \overline{h}(\overline{x}))\right) \partial_{\overline{x}} \overline{h}(x), \tag{5}$$

where $\overline{u}(\overline{x}, \overline{z})$ is the horizonatl wind disturbance. In (4)-(5)

$$\overline{U}(\overline{z}) = \tanh\left(\frac{\overline{z}}{\sqrt{J}}\right), \text{ and } \overline{h}(\overline{x}) = \frac{H_N}{1 + \overline{x}^2/2F_r^2} \tag{6}$$

where

$$J = \frac{N^2 d^2}{U_\infty^2}, \; H_N = \frac{HN}{U_\infty}, \quad \text{and } F_r = \frac{LN}{U_\infty} \tag{7}$$

are the surface and minimum Richardson number, a non-dimensional mountain height, and a Froude number respectively. Still in (4) the dissipative vertical scale for each harmonics,

$$\overline{z}_k = \frac{\overline{z}_b}{2}\left(\frac{1}{F_r\overline{k}} + F_r\overline{k}\right). \tag{8}$$

has been expressed in terms of a global scale $\overline{z}_b$, with the first term in parenthesis resulting from Rayleigh drag and Newtonian cooling of coefficient $\overline{z}_b/F_r * \sqrt{J}/2$ and the second term from a viscous dissipation which acts in the x-direction only of coefficient $\overline{z}_b F_r/\sqrt{J}/2$ (see also the right hand sides of Eqs.4 in L16). They are introduced to regularize the critical level

dynamics for all the harmonics, i.e. the longer and the shorter ones respectively. Note that $\overline{z}_k$ is written differently than in L16 to make clear that when the formula is applied to the dominant wavenumber Fr^{-1}, $\overline{z}_k$ in (8) compares to the dissipative scale $\overline{z}_b$[1].

To construct $\hat{w}_c$, L16 uses for each k an exact solution of the inviscid version of (4), $\hat{w}_{\rm inv}(\overline{k},\overline{z})$, which is based on hypergeometric functions (see [Lott *et al.*(1992)] and (34) in L16), and which asymptotic behaviors are

$$\hat{w}_{\rm inv}(\overline{k},\overline{z} >> 1) \approx e^{-\overline{m}\,\overline{z}/\sqrt{J}}, \tag{9}$$

$$\hat{w}_{\rm inv}(\overline{k},\overline{z} << 1) \approx a_1(\overline{k})\overline{z}^{1/2-i\mu} + a_2(\overline{k})\overline{z}^{1/2+i\mu} \tag{10}$$

where,

$$\overline{m} = \sqrt{J}\sqrt{|\overline{k}^2 - 1|},\ \mu = \sqrt{|J - \frac{1}{4}|}, \tag{11}$$

and where $a_1(\overline{k})$ and $a_2(\overline{k})$ have analytical forms once the "unit" amplitude condition (9) is satisfied. Also, when $\overline{k}^2 < 1$, $\overline{m}$ is changed in $-i{\rm sign}(\overline{k})\overline{m}$, where the sign is to ensure upward group speed. Near the surface, L16 also uses the asymptotic solution of the damped Taylor-Goldstein Equation (4) valid when $\overline{z} << 1$:

$$\hat{w}_{\rm srf}(\overline{k},\overline{z}) = a_1(\overline{k})(\overline{z} - \overline{z}_k)^{1/2-i\mu} + a_2(\overline{k})(\overline{z} - \overline{z}_k)^{1/2+i\mu}, \tag{12}$$

where a_1 and a_2 are the same as in (10) to ensure matching. To establish how these aproximate solutions can be combined to provide a uniformly valid approximation of $\hat{w}_c(\overline{k},\overline{z})$, Fig. 1 shows $\hat{w}_{\rm inv}(\overline{k},\overline{z})$ (thin solid), its approximation near $z = 0$ ((10), thick dashed) and $\hat{w}_{\rm srf}(\overline{k},\overline{z})$ (thick dashed and dots). For the three values of J selected, $J = 0.5, 2, 4$, we see that below around $z \approx J/4$ the inviscid exact solution $\hat{w}_{\rm inv}$ and its inviscid approximation on the right of (10) almost coincide whereas above this altitude the asymptotic damped approximation ($\hat{w}_{\rm srf}$ in (12)) and the asymptotic inviscid solutions (10) are very close. This suggests that we can take the altitude $J/4$ to make a transition between the exact inviscid solution and the asymptotic damped solution. In the following, this transition is made by patching these two functions using *tanh* tapers centered at $\overline{z} = J/4$ and of depth $\Delta\overline{z} = J/5$, i.e. by writting,

$$\hat{w}_c(\overline{k},\overline{z}) = \frac{\left(1 + \tanh\left(\frac{5\overline{z}}{J} - \frac{5}{4}\right)\right)}{2}\hat{w}_{\rm inv}(\overline{k},\overline{z}) + \frac{\left(1 - \tanh\left(\frac{5\overline{z}}{J} - \frac{5}{4}\right)\right)}{2}\hat{w}_{\rm srf}(\overline{k},\overline{z}). \tag{13}$$

The thick gray curves in Figs. 1a, b, c show these new approximations, and illustrate how well they behave for all $\overline{z}$, permitting a smooth passage from the damped solutions near the ground to the exact inviscid one in the far-field. Compared to L16, we use this approximation in the inversion of (5),

$$\int_{-\infty}^{+\infty} f(\overline{k})\left[\hat{w}_c(\overline{k},\overline{h}) - \hat{u}_c(\overline{k},\overline{h})\frac{dh}{dx}\right] e^{i\overline{k}\overline{x}}d\overline{k} = U\frac{dh}{dx} \tag{14}$$

rather than using (12) to express $\hat{w}_c$ and $\hat{u}_c$ in the terms between brackets in (14). This formally permits to consider more elevated ridges than in L16.

[1]For consistency, note also that the boundary layer depth $\overline{z}_B$ used in L16 is related to the one here by $\overline{z}_B = 5\overline{z}_b$.

3 A dry foehn mechanism

As the numerical results obtained with this new formulation of the model are consistent with those in L16 we will only emphasize on the descents of warm air that characterize foehn. In the following we take a domain of length 800 spanned by 1024 equally spaced points, the Froude number $F_r = 5$ and the boundary layer scale $\overline{z}_b = 0.05$. The three panels in the left column of Fig. 2 shows that when J increases the foehn effect increases, as expected from the results in L16, where the same behavior was discussed in terms of downslope windstorms. The reader is referred to this paper for more complete sensitivity tests to H_N and $\overline{z}_b$, but it is worthwhile to note here that when J passes 1 typically, an isentropic surface initially at the altitude of the ridge is not much displaced upward when it approaches the ridge but easily reaches the surface along the downslope side of the ridge (lowest dashed line in Fig. 2c). This "foehn" effect becomes extremely pronounced when $J = 4$ in Fig. 2e: almost all the air located between $H_N < \overline{z} < 2H_N$ upstream of the ridge descent below the mountain top $\overline{z} < H_N$ in the lee-side. Near the surface downstream, the theory predicts highly distorted isentropes and potential temperatures that are below the minimum value upstream: this is not realistic so they are not shown but this indicates where the dynamics may trigger breaking.

If the foehn effect proposed is purely related to the critical level dynamics, then it should be present in a theory that is even simpler than the one used to produce the panels on the left in Fig. 2. For this purpose we next derive the theory when the wind shear U_z and buoyancy frequency are both constant, in the hydrostatic approximation and when the boundary layer depth is identical for all harmonics $\overline{z}_k = \overline{z}_b$. As we will see in this "constant shear" case we can also formally eliminate the reflected waves, proving that they also play a minor role. To make clear that the dynamics in this case is only controlled by J and $\overline{z}_b$, the two parameters that control the critical level dynamics, we introduce a scaling suited to the constant wind shear configuration by taking for the horizontal and vertical scales those of the mountain. We also scale the horizontal velocity disturbance by the background velocity at the mountain top,

$$x = L\tilde{x}, z = H\tilde{z}, u = U_z H\tilde{u}, w = U_z H^2/L\tilde{w}, p = \rho_r U_z^2 H^2 \tilde{p}, \text{ and } b = U_z^2 H\tilde{b}. \tag{15}$$

In this new set-up and scaling, the Boussinesq dynamics writes

$$\tilde{z}\partial_{\tilde{x}}\tilde{u} + \tilde{w} = -\partial_{\tilde{x}}\tilde{p},\ \partial_{\tilde{z}}\tilde{p} = \tilde{b},\ \tilde{z}\partial_{\tilde{x}}\tilde{b} + J\tilde{w} = 0, \tag{16a}$$

$$\partial_{\tilde{x}}\tilde{u} + \partial_{\tilde{z}}\tilde{w} = 0,\ \tilde{w}(\tilde{z} = \tilde{h}) = \left(\tilde{h} + \tilde{u}\right)\frac{\partial \tilde{h}}{\partial \tilde{x}}, \tag{16b}$$

$$\tilde{h} = \frac{1}{1 + \tilde{x}^2/2}, \tag{16c}$$

it is only controlled by the Richardson number J. In this setup, we know that for each harmonics the vertical velocity is exactly,

$$\hat{w} = \tilde{z}^{1/2 + i\text{sign}(\tilde{k})\mu}, \tag{17}$$

where we have only retain the upward propagating solution [Booker and Bretherton(1967),]: there is no reflected wave by construction. We then incorporate a dissipative scale $\tilde{z}_k = \tilde{z}_b$ which we also take constant, a simplification that permits to define a canonical solution

$$\hat{w}_c(\overline{z}, \overline{k}) = \left(\tilde{z} - i\text{sign}(\tilde{k})\tilde{z}_b\right)^{1/2 + i\text{sign}(\tilde{k})\mu}. \tag{18}$$

We will next use this solution to evaluate the wave field in (3) and the boundary condition in (5). To ease comparison, the results will be shown using the dimensionless variables of the more complete theory,

$$\overline{x} = F_r\tilde{x}, \overline{z} = H_N\tilde{z}, \overline{u} = \frac{H_N}{\sqrt{J}}\tilde{u}, \overline{w} = \frac{H_N^2}{F_r\sqrt{J}}\tilde{w}. \tag{19}$$

The results from the simplified theory are shown in the right panels of Fig. 2, the resolutions being identical to those used to build the corresponding panels on the left. To have comparable results nevertheless we have taken a boundary layer scale that is smaller than that used in Section 2, $\overline{z}_b = 0.02$, a difference that is only related to our choice to take a constant boundary layer scale (if we adopt the formula (8) we need to return to the value $\overline{z}_b = 0.05$ to obtain the same results). With this scale, the simplified theory gives almost exactly the same results as the more complete one, at least at low level. As we emphasized previously, in this simplified theory, there is no reflected waves by construction, proving that the onset of foehn can be entirely due to the near surface critical level dynamics i.e. a mechanism summarized mathematically by (18), a mechanism that exclude pre-conditionning of a well mixed layer by upper level wave breaking, non-linear and now linear wave reflections.

Finally to understand further why the near-surface critical level dynamics makes the foehn so sensitive to J it is worthwhile to notice that for large J, the [Booker and Bretherton(1967)]'s solution (17) has an interpretation in terms of vertical wavenumber. To make this transparent we approximate it near the mountain top by writing $\overline{z} = H_N + \delta\overline{z}$, which yields

$$\overline{z}^{1/2+i\mu} = \overline{z}^{1/2}e^{i\mu\ln\overline{z}} \approx \overline{z}^{1/2}H_N^{i\mu}e^{i\frac{\mu}{H_N}\delta\overline{z}}. \tag{20}$$

Near the mountain top, the disturbance has a characteristic wavenumber $\overline{m} \approx \mu/H_N$. Now, we know that mountain flow dynamics becomes nonlinear when the disturbance's vertical wavelength $\overline{m}^{-1}$ becomes smaller than the mountain height H_N. The argument often given is that in this case the linear theory predicts that vertical velocities change sign before the air parcels reach the mountain top. If we apply this condition here, we have that nonlinear effect become large when $H_N/\mu < H_N$, which approximately simplifies to the condition $J > 1$, which is the condition that favors foehn in the theory here and the downslope winds in L16.

Another point we make is that foehn is not associated with upper level wave breaking, i.e. that some form of wave breaking can occur below the mountain top without occurring aloft. To illustrate this qualitatively we next use the same line of arguments as before. We compare the wave vertical wavelength $\overline{m}_B$ and the vertical displacement $\overline{\eta}_B$ produced by the wave around a "breaking" altitude H_B, yet to be found, and by writing $\overline{z} = H_B + \delta\overline{z}$. This yields

$$\overline{m}_b \approx \mu/H_B \text{ and } \overline{\eta}_B \approx H_B^{-1/2+i\mu}H_N^{3/2-i\mu}. \tag{21}$$

respectively. Qualitatively, breaking occurs when $|\overline{\eta}_B| \geq \overline{m}_B^{-1}$, which gives,

$$H_B \leq \mu^{2/3}H_N. \tag{22}$$

Wave breaking is confined to the lowest layers, and inhibited above the mountain summit H_N at least when $\mu < 1$. This is the basic reason due to which the foehn mechanism described here is not associated with upper level wave breaking. Of course this effect simply translates the fact that in presence of shear, the vertical wavelength increases with altitude.

The result in (22) also illustrates that the depth of the layer over which breaking occurs increases with J. To a certain extent this suggests that the dissipative layer depth should increase with J. As we will see next this is in fact the case when we compare to fully nonlinear simulations.

4 Verification with fully nonlinear model

To extend the above results beyond the inflow-linear and Boussinesq approximations, we next use the WRF model in the 2D mountain flow configuration available on line[2][Skamarock *et al.*(2008),]. It is configured here for a 100km long and 12km height domain gridded by 1000×1000 points yielding resolutions of 100m and 12m in the horizontal and vertical directions respectively. At the lateral bounds the domain is open and below the model top a 6km deep absorbing layer prevents the gravity waves to be reflected downward. These quite high resolutions are to ensure that the near surface critical level dynamics is well represented. They require a time step $\Delta t = 0.5$s. Note also that all the results from WRF shown next have been verified against simulations where the horizontal and vertical gridspacing are divided by two. As the WRF model is fully compressible, it is mandatory to recall that in it the stratification is represented by a Brunt Vaisala frequency given by $N^2 = \frac{g}{\theta_0}\frac{d\theta_0}{dz}$, where θ_0 is a background potential temperature. To ensure that it is constant and to minimize the vertical variations of the background fields that could result in partial reflections, we consider an isothermal atmosphere $T_r = 290$K, yielding $N^2 = \frac{\kappa g^2}{RT_r} = 3.10^{-4}\text{s}^{-2}$, where κ, R, and g have their conventional dry air and earth-values. We will then impose the background wind (1) and always take $U_\infty = 10$m/s, the minimum Richardson number will then be changed by varying the shear layer depth d. Also, the mountain height will be given by (2) with $L = 2.8$km to ensure $F_r = 5$.

Finally, in all the WRF simulations presented the dissipative coefficients are set to 0 and the surface boundary condition is free slip. This does not mean that the simulations are inviscid, because irreversible and diabatic processes will necessarily occur if the model confirms the onset of convective overturnings like those found in the theoretical model in the previous section. All the experiments presented in the next section prove that the WRF dynamical core is stable and dissipative enough to handle these irreversible processes. When we return to the theory, it is a priori difficult to say how these irreversible processes can be translated in the theorety. Nevertheless, as the theory has a free parameter to represent dissipations, the boundary layer scale $\overline{z}_b$, we can vary it and try to identify a value for which there is a match between the nonlinear simulations and the theory. To sort out this issue we have undertaken a systematic comparison between the WRF model and the theoretical one, varying the boundary layer depth in the latter. We found a good agreement when we take a boundary layer depth varying like

$$\overline{z}_b/\sqrt{J} = 0.05. \tag{23}$$

The 0.05 factor is purely empirical and little sensitive to the resolution in both models, but the $\sqrt{J}$ term suggests that between the simulations and the theory, the penetration of the boundary layer depth into the shear layer needs to be the same.

[2] www2.mmm.ucar.edu/wrf/users/downloads.html

4.1 Fixed mountain height

To confirm that theory can match the fully nonlinear simulation, we present experiments with a fixed mountain height $H = 250$m, ($H_N = 0.5$), and vary the minimum Richardson number between $J = 0.5$ and $J = 5$. Figure (3) shows the horizontal wind disturbances from the linear model (left) and the WRF model (right) for 3 different Richardson numbers ($J = 0.5$, 2, and 4). In each figure the contour interval is proportional to the background wind amplitude at the top of the Hill ($\approx H_N/\sqrt{J}$), a value representative of the disturbance amplitude needed to satisfy the lower boundary condition. The first striking result is that the left hand and right hand panels share strong similarities: the wave amplitude and phase line tilts with altitude are comparable. Also, when J increases, the phase line tilts with altitude become more and more vertical above the ridge, which means that the characteristic horizontal scale of the wave field decreases when J increases: this behavior is consistently reproduced by the theory and by the WRF model. In all panels, we also note that the horizontal wind disturbances are substantially larger on the downstream side ($\overline{x} > 0$). This upstream/downstream difference becomes very pronounced near the ground, contrasting the two flanks of the mountain. It is this difference in horizontal winds that explains why low level shears can produce intense downslope winds (L16), and we see here that it is also present in the simulations.

Returning to the foehn effect, Fig. 4 shows the isentropic surfaces corresponding to the experiments shown in Fig. 3. Again, the results between the theory and WRF are quite consistent, some qualitative discrepancies emerge downstream where the simulations start to predict potential temperature jumps. These figures also illustrate another feature: the theoretical results shown in Fig. 2 and in Fig. 4 differ by the value of $\overline{z}_b$, which increases with J for the comparison with WRF (see eq. 23). Comparison of figures 2 and 4 shows that the increase of $\overline{z}_b$ limits the onset of foehn.

4.2 Fixed penetration of the mountain into the shear

As said before, to match the WRF simulations, we had to keep constant in the theoretical model, the ratio between the shear layer depth $\sqrt{J}$ and the boundary layer scale $\overline{z}_b$. This limits the amplitude of foehn in the theoretical model, but does not make it disappear. To make the Foehn effect more evident in the simulations, we next keep the "penetration" of the mountain into the shear constant between the experiments by keeping $H_N/\sqrt{J}$ constant. In this case, at the top of the hill, the incident wind is the same in all the experiments, and to a certain extent, it is only the stratification that is changed. Note also that in these experiments the ratio between the boundary layer depth and the mountain height $\overline{z}_b/H_N$ is also constant, which allows cleaner comparisons of results since z_b now changes with $\sqrt{J}$.

The results are shown in Fig. 5 for ($J = 0.5$, $H_N = 0.25$) and ($J = 4$, $H_N = 0.71$), the corresponding plots for ($J = 2, H_N = 0.5$) being already in Figs 4c–d. Again, a good match between the theory and WRF is found, which is important since we are now using non-dimensional mountain height that are near 1. In both the theoretical model and in WRF, the foehn downstream is now slightly more substantial when $J = 4$ than when $J = 0.5$, but the difference are more in terms of horizontal distance over which the air descends on the lee-side. In the simulation with $J = 4$ the isentrope which is at the altitude of the mountain summit upstream rapidly descends below half the mountain top downstream, before returning to its upstream altitude after the passage through an hydraulic jump. Importantly both this behavior

and the location of the jump are well predicted by the theory. When $J = 0.5$ the descent of air in WRF is less abrupt, in agreement with theory but the total descent is still about half the mountain height. Another point is worth noticing. In Figs. 5a-d, but this is also true in all the other Figures, there is very little uplift of the air parcels in front of the ridge, the most spectacular vertical displacements occur after the passage of the summit. This small uplift could suggest that diabatic effects should not much affect the results, at least when the atmosphere is not close to water vapor saturation.

In this paper we try to make the point that upper level wave breaking is not needed for foehn to occur. The basic argument is that the theory is linear, yet shows a very good agreement with the fully non linear simulations. Nonetheless, we can go one step further and diagnose if upper level wave breaking actually occurs in WRF and in the theory. The answer is simply that it does not,and to illustrate this the Figs. 5e-f display the isentropic surfaces over a much larger domain than in Figs. 5c–d. In no place, except in the downstream lee side, the isentropes become almost vertical. This is in contrast with what is found with the Long's model with uniform U (see Fig. 1f in L16). In it, downslope winds and foehn always occur in conjunction with upper level wave breaking.

5 More systematic comparisons and alternative configurations

5.1 Quantitative indices

To provide quantitive measures of our results we have built global indices characterizing our problem and conducted 64 pairs (theory versus WRF) of experiments, 32 corresponding to the constant height cases described in *4.1.* and 32 to the constant penetration of the mountain into the shear cases described in *4.2.* For the first index, we follow L16 and measure downslope windstorm intensity by,

$$A = \underset{\substack{\overline{z}<H_N/2 \\ 0<\overline{x}<5F_r}}{Max} \left(\frac{\overline{u}(\overline{x},\overline{z})}{U(H_N/\sqrt{J})} \right). \tag{24}$$

The index A indicates to which extent the wind in the flow along the foothills (defined as the region with $z < H_N/2$ and $0 < x < 5F_r$) exceeds the background wind at the top of the hill ($U(H/d)$). In terms of foehn it is an important index because when the descent is rapid there is less time for diabatic effects to mitigate the warming of the air masses. The results in Fig. 6a somehow reproduce those in L16: the downslope wind intensity increases with stability J. However the increases are not as spectacular as in [Lott(2016)] where A much more easily reaches values above 1, but this is consistent with the fact that z_b increases with J. This constraint is the price to pay for our theory to be consistent with the simulations.

As our theory reproduces mountain waves quite well (see Fig 3), we have also evaluated the wave stress in $z = 2\sqrt{J}$ (that is well above the maximum mountain height and the low level shear) and compare it to the linear hydrostatic wave drag produced by the mountain in (6) in a uniform flow of intensity $U(H_N) = \frac{H_N}{\sqrt{J}}$:

$$F^z = -\frac{\int_{-\infty}^{\infty} \overline{u}\,\overline{w}\,d\overline{x}}{\frac{\pi}{4}\frac{H_N^3}{\sqrt{J}}}. \tag{25}$$

Again, the curves in Fig.6b show that the theory and the nonlinear simulations are in good agreement. Interestingly, when the penetration of the mountain into the shear stays constant and J increases, the normalized wave stress F^z increases well beyond 1. This behavior is reminiscent of the high drag states often found in non linear mountain flow theory [Bacmeister and Pierrehumbert(1988),].

Finally, to characterize foehn, we identify the highest altitude from which are coming the isentropic surfaces that arrive along the downstream foothill, and normalize by the mountain maximum altitude. In our non-dimensional formalism where the background potential temperature varies as $\overline{z}$ exactly, this is conservatively given by,

$$F_{hn} = \underset{\substack{\overline{z}<H_N/2 \\ 0<\overline{x}<5F_r}}{Max} \left(\frac{\overline{\theta}+\overline{z}}{H_N} \right). \tag{26}$$

Interestingly, in our models this factor is always near 1. In other words the dynamics forces isentropic surfaces that are upstream at the altitude of the ridge to descend along the foothills downstream. Hereagain simulations and theory compare well. In both, the foehn intensity increases with J, but as for the downslope winds intensity, it is less pronounced than when z_b is kept small and constant in the theory (not shown).

5.2 Alternative configurations

In the real atmosphere the low level shears have at least two causes: the thermal gradients due to the presence of fronts and the effect of the boundary layer. The first imposes shears that extend well above the boundary layer, the second forces the winds to vanish at the surface. There is no reason, except simplicity, to consider that the shears associated with these two processes have similar values. In this sense, we could say that our almost inviscid interpretation of the wave dynamics above the boundary layer is only adapted to the shears produced via thermal wind balance, Raighleigh friction and Newtownian cooling being an ad hoc parameterizations of the boundary layer absorptive properties, an absorption that becomes very efficient when the incident wind is null at $z = 0$. To show that our results have more generality than this apparently "ad-hoc" setup, we next propose three experiments. In the first two, we keep the same models and setup as in Figs. 5c and 5d but shift vertically the mountain height by $H_N/10$, e.g. by writing,

$$\overline{h}(\overline{x}) = \overline{h} = \frac{H_N}{1+\overline{x}^2/2F_r^2} + \frac{H_N}{10}. \tag{27}$$

Doing so there is no need to rewrite the theory but, from a dynamical point of view there is a major change: the incident wind is no longer exactly null at the surface. The results in Figs. 7a and 7b show that in this case the theory and WRF simulations are still consistent and that the foehn effects are almost identical to those when when the incident wind is null at $z = 0$ in Figs. 5c and 5d respectively.

In the third experiment, we return to the exact setup of WRF used in Fig. 5d, but instead of the free slip boundary layer condition we adopt a planetary boundary layer scheme that has been extensively used in WRF. The chosen configuration activates the vertical diffusion described in [Hong and Pan(1996)] with the surface conditions evaluated using similarity theory. At the surface we impose a constant potential temperature, with value equal to the upstream temperature value at $z = 0$ and take a roughness length $z_0 = 10$cm. The results for the

potential temperature and after a non-dimensional time $\bar{t} \approx 100$, are shown in Fig. 7c. Again the results in term of foehn compare well with those in Fig. 5d, and this despite the fact that now the low level winds and temperature adapt themselves to more conventional surface boundary conditions.

6 Discussion

The central result of this paper is the resemblance between Fig.5c and Fig.5d. It shows that isentropic "drawdown", a dry mechanism of foehn, where air parcels do not ascend significantly on the upstream side of mountains before descending abruptly on the lee side can be produced in a model without inflow nonlinear effects. The mechanism at work is related to the near surface critical level dynamics that occurs for mountain waves, the critical level being located just below the lower boundary. In this case, the inflow linear dynamics anticipate well where the wave breaks as is often the case in gravity wave theory. Not surprisingly, in the presence of low level wind shear, mountain wave breaking is favored in regions located below the mountain top rather than above.

In essence, the results obtained illustrate the significance of low level wind shears and stability on mountain flow dynamics, something often noticed in mountain meteorology, at least in the context of trapped lee waves [Reinecke and Durran(2009), Georgelin and Lott(2001),]. In this context it is interesting to note that there are many field experiments where upstream soundings show low level shears [Doyle *et al.*(2011), Sheridan *et al.*(2007),], generally related to advancing fronts [Lothon *et al.*(2003),], when the low level shear is associated with thermal wind balance. It is also worth noticing that there are cases where foehn is observed in the absence of upper level wave breaking [Flamant *et al.*(2002)]. Other aspects of the theory also have reasonable behavior. According to [Richner and Hachler(2013)] a forecaster's rule says that foehn winds rarely descend more than 2000m below the mountain crest. In all figures when the foehn is strong (for instance when $J \geq 2$ in Figs. 4–5) we note a comparable behavior, the foehn never extend down to $z = 0$ in the lee side in these cases. Also, downstream where the isentropic surface become vertical, there is always near the surface a pool of relatively cold air. It is interesting that such a pool has often been viewed as an active part of the foehn dynamics [Lothon *et al.*(2003),], we see here that it can be a consequence of it.

All these remarks are not to say that we want here to replace the existing theories of adiabatic foehn by a completely new one, the message is rather to complement them. Actually, our upstream low level shear can be viewed as a form of blocking, since it imposes slow incident low level flows. Also, upper level mountain wave breaking tend to decelerate the low level flow, again our background profiles with slow low level winds can be viewed as a result of this process. Finally, our results show that linear models forced by a nonlinear boundary condition potentially have some skill, which can turn out to be useful since simplified linear models are still sometimes used to predict mountain wave operationally at a cheap numerical cost [Vosper(2003), Sheridan *et al.*(2017),]. Finally, one may note that the equations solved in the numerical simulations and in the linear theory differ in their treatment of boundary layer dissipation. For consistency one may wish that the WRF model and the theory be adapted to use the same dissipative processes. Nevertheless, we explored in Section 5 the sensitivity of the results to the precise boundary condition at the surface (non-zero surface wind or including a boundary layer parameterization) and these tests suggested that the foehn effects are robust to

such changes.

Acknowledgements

This work was supported by the European Commission's project ARISE2 (Grant Agreement 653980) and the Comissariat à l'Energie Atomique (CEA).

References

[Bacmeister and Pierrehumbert(1988)] Bacmeister JT, Pierrehumbert RT. 1988. On high drag states of nonlinear stratified flow over an obstacle. *J. Atmos. Sci.* **45**: 63–80.

[Baines (1998)] Baines PG. 1998. *Topographic effects in stratified flows*. Cambridge University Press.

[Booker and Bretherton(1967)] Booker JR, Bretherton FP. 1967. The critical layer for internal gravity waves in a shear flow. *J. Fluid Mech.* **27**: 102–109, doi:http://dx.doi.org/10.1017/S0022112067000515.

[Brinkmann(1974)] Brinkmann WAR. 1974. Strong downslope winds at boulder, colorado. *Mon. Wea. Rev.* **102**: 592–602.

[Cannon *et al.*(2017)] Cannon F, Carvalho LMV, Jones C, Hall T, Gomberg D, Dumas J, Jackson M. 2017. Wrf simulation of downslope wind events in coastal santa barbara county. *Atmos. Res.* **191**: 57–73, *Atmos. Res.* **191**: 57–73, doi:10.1016/j.atmosres.2017.03.010.

[Doyle *et al.*(2011)] Doyle JD, Gabersek S, Jiang Q, Bernardet L, Brown JM, Dornbrack A, Filaus E, Grubisic V, Kirshbaum DJ, Knoth O, Koch S, Schmidli J, Stiperski I, Vosper S, Zhong S. 2011. An intercomparison of t-rex mountain-wave simulations and implications for mesoscale predictability. *Mon. Wea. Rev.* **139**: 2811–2831, doi:http://dx.doi.org/10.1175/MWR-D-10-05042.a.

[Drobinski and Coauthors(2007)] Drobinski P, Coauthors. 2007. Foehn in the rhine valley during map: A review of its multiscale dynamics in complex valley geometry. *Quart. J. Roy. Meteor. Soc.* **133**: 897916.

[Durran(1990)] Durran DR. 1990. Mountain waves and downslope winds. *AMS Meteorological Monographs* **23**: 59–83.

[Elvidge and Renfrew(2016)] Elvidge AD, Renfrew IA. 2016. The causes of foehn warming in the lee of mountains. *Bull. Amer. Meteor. Soc.* **97**(3): 455–466.

[Elvidge *et al.*(2015)] Elvidge AD, Renfrew IA, King JC, Orr A, Lachlan-Cope TA, Weeks M, Gray SL. 2015. Foehn jets over the larsen c ice shelf, antarctica. *Quarterly Journal of the Royal Meteorological Society* **141**(688): 698–713.

[Flamant *et al.*(2002)] Flamant C, Drobinski P, Nance L, Banta R, Darby L, Dusek J, Hardesty M, Pelon J, Richard E. 2002. Gap flow in an alpine valley during a shallow south fhn event: Observations, numerical simulations and hydraulic analogue. *Quart. J. Roy. Meteor. Soc.* **128**(582): 1173–1210, doi:10.1256/003590002320373256.

[Georgelin and Lott(2001)] Georgelin M, Lott F. 2001. On the transfer of momentum by trapped lee waves. case of the iop3 of pyrex. *J. Atmos. Sci.* **58**: 3563–3580.

[Hong and Pan(1996)] Hong SY, Pan HL. 1996. Nonlocal boundary layer vertical diffusion in a medium-range forecast model. *Mon. Wea. Rev.* **124**: 2322–2339.

[Hunt *et al.*(1988a)] Hunt JCR, Leibovich S, Richards KJ. 1988a. Turbulent shear flows over low hills. *Quart. J. Roy. Meteor. Soc.* **114**: 1435–1470.

[Hunt *et al.*(1988b)] Hunt JCR, Richards KJ, Brighton PWM. 1988b. Stably stratified shear flow over low hills. *Quart. J. Roy. Meteor. Soc.* **114**: 859–886.

[Laprise and Peltier(1989)] Laprise R, Peltier WR. 1989. On the structural characteristics of steady finite-amplitude mountain waves over bell-shaped topography. *J. Atmos. Sci.* **26**: 586–595.

[Lilly and Klemp(1979)] Lilly DK, Klemp JB. 1979. The effects of terrain shape on nonlinear hydrostatic mountain waves. *Journal of Fluid Mechanics* **95**(2): 241261, doi:10.1017/S0022112079001452.

[Long(1953)] Long RR. 1953. Some aspects of the flow of stratified fluids; 1. a theoretical investigation. *Tellus* **5**: 42–58.

[Lothon *et al.*(2003)] Lothon M, Druilhet A, Bnech B, Campistron B, Bernard S, Sad F. 2003. Experimental study of five fhn events during the mesoscale alpine programme: From synoptic scale to turbulence. *Quarterly Journal of the Royal Meteorological Society* **129**(592): 2171–2193, doi:10.1256/qj.02.30, URL http://dx.doi.org/10.1256/qj.02.30.

[Lott(2007)] Lott F. 2007. The reflection of a stationary gravity wave by a viscous boundary layer. *J. Atmos. Sci.* **139**: 3363–3371, doi:http://dx.doi.org/10.1175/JAS4020.1.

[Lott(2016)] Lott F. 2016. A new theory for downslope windstorms and trapped lee waves. *J. Atmos. Sci.* **73**: 3585–3597, doi:doi:10.1175/JAS-D-15-0342.1.

[Lott *et al.*(1992)] Lott F, Kelder H, Teitelbaum H. 1992. A transition from kelvin-helmholtz instabilities to propagating wave instabilities. *Physics of Fluids A* **4**: 1990–1997, doi:http://dx.doi.org/10.1063/1.858368.

[McGowan *et al.*(2002)] McGowan HA, Sturman AP, ans P Zawar-Reza MK. 2002. Observations of foehn onset in the southern alps, new zealand. *Meteor. Atmos. Phys.* : 215–230.

[Miltenberger *et al.*(2016)] Miltenberger AK, Reynolds S, Sprenger M. 2016. Revisiting the latent heating contribution to foehn warming: Lagrangian analysis of two foehn events over the swiss alps. *Quarterly Journal of the Royal Meteorological Society* **142**(698): 2194–2204.

[Muraki(2011)] Muraki DJ. 2011. Large-amplitude topographic waves in 2d stratified flow. *J. Fluid Mech.* **681**: 172–192, doi:10.1017/jfm.2011.187.

[Reinecke and Durran(2009)] Reinecke PA, Durran DR. 2009. Initial-condition sensitivities and the predictability of downslope winds. *J. Atmos. Sci.* **66**: 3401–3418, doi:http://dx.doi.org/10.1175/2009JAS3023.1.

[Richner and Hachler(2013)] Richner H, Hachler P. 2013. Understanding and forecasting alpine foehn. *Mountain Weather and Forecasting* : 219–260doi:10.1007/978-94-007-4098-3_4.

[Seibert *et al.*(2000)] Seibert MR, Feldman H, Neininger B, Baumle M, Trickl T. 2000. South foehn and ozone in the eastern alps - case study and climatological aspects. *Atmospheric Environment* : 1379–1394.

[Seibert(1990)] Seibert P. 1990. South foehn studies since the alpex experiment. *Meteor. Atmos. Phys.* : 91–103.

[Seibert(2005)] Seibert P. 2005. Hanns thermodynamic foehn theory and its presentation in meteorological textbooks in the course of time. *From Beaufort to Bjerknes and Beyond, Algorismus* **52**: 169–180.

[Sharples *et al.*(2010)] Sharples JJ, Mills GA, McRae RHD, Weber RO. 2010. Foehn-like winds and elevated fire danger conditions is southeastern australia. *J. Appl. Meteor. Climatol.* **49**: 1067–1095, doi:10.1175/2010JAMC2219.1.

[Sheridan *et al.*(2017)] Sheridan P, Vosper S, Brown P. 2017. Mountain waves in high resolution forecast models: Automated diagnostics of wave severity and impact on surface winds. *Atmosphere* **8**(1): 24.

[Sheridan *et al.*(2007)] Sheridan PF, Horlacherxi V, Rooney GG, Hignett P, Mobbs SD, Vosper S. 2007. Influence of lee waves on the near surface flow downwind of the pennines. *Quart. J. Roy. Meteor. Soc.* **133**: 1353–1369, doi:10.100a/2qj.110.

[Skamarock *et al.*(2008)] Skamarock WC, Klemp JB, Dudhia J, Gill DO, Barker DM, Duda MG, Huang XY, Wang W, Power JG. 2008. A description of the advanced research wrf version 3. *NCAR Tech. Note* : 113ppdoi:doi:10.5065/D68S4MVH.

[Smith and Skyllingstad(2011)] Smith CM, Skyllingstad ED. 2011. Effects of inversion height and surface heat flux on downslope windstorms. *Mon. Wea. Rev.* **139**: 3750–3764, doi:http://dx.doi.org/10.1175/2011MWR3619.1.

[Smith(1985)] Smith RB. 1985. On severe downslope winds. *J. Atmos. Sci.* **42**: 2597–2603, doi:http://dx.doi.org/10.1175/1520-0469(1985)042⟨2597:OSDW⟩2.0.CO;2.

[Smith *et al.*(2003)] Smith RB, Jiang Q, Fearon MJ, Tabary P, Dorninger M, Doyle JD, Benoit R. 2003. Orographic precipitation and air mass transformation: An alpine example. *Quart. J. Roy. Meteor. Soc.* **129**: 433–454, doi:10.1256/qj.01.212.

[Takane and Kusaka(2011)] Takane Y, Kusaka H. 2011. Formation mechanisms of the extreme high surface air temperature of 40.9c observed in the tokyo metropolitan area: Considerations of dynamic foehn and foehnlike wind. *J. Appl. Meteor. Climatol.* **50**: 1827–1841, doi:DOI:10.1175/JAMC-D-10-05032.1.

[Vergeiner(1971)] Vergeiner I. 1971. An operational linear lee wave model for arbitrary basic flow and two-dimensional topography. *Quart. J. Roy. Meteor. Soc.* **97**(411): 30–60.

[Vosper(2003)] Vosper SB. 2003. Development and testing of a high resolution mountain-wave forecasting system. *Meteorological Applications* **10**(1): 75–86.

[Wursch and Sprenger(2015)] Wursch M, Sprenger M. 2015. Swiss and austrian foehn revisited: A lagragian based analysis. *Meteorologische Zeischrift* **24**: 225–242.

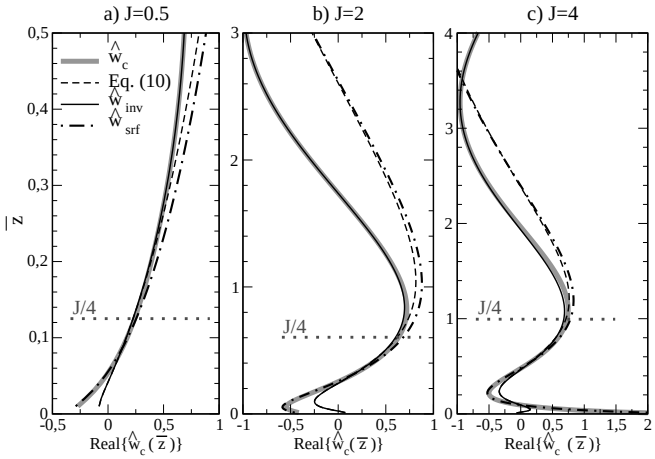

Figure 1: Vertical profiles of the solutions used to build the canonical solution: inviscid exact solution $\hat{w}_{\rm inv}(\overline{k},\overline{z})$ (black solid), approximation of $\hat{w}_{\rm inv}(\overline{k},\overline{z})$ near $\overline{z}=0$ (right of (10), black dashed), damped approximation $\hat{w}_{\rm surf}$ (12, black dashed and dot), and approximation of $\hat{w}_c(\overline{k},\overline{z})$ (thick gray). In all panels, only the real part of the complex functions are shown, $\overline{k}=0.1$ and $\overline{z}_b=0.05$ for $J=0.5,2$, and 4 in a) b) and c) respectively.

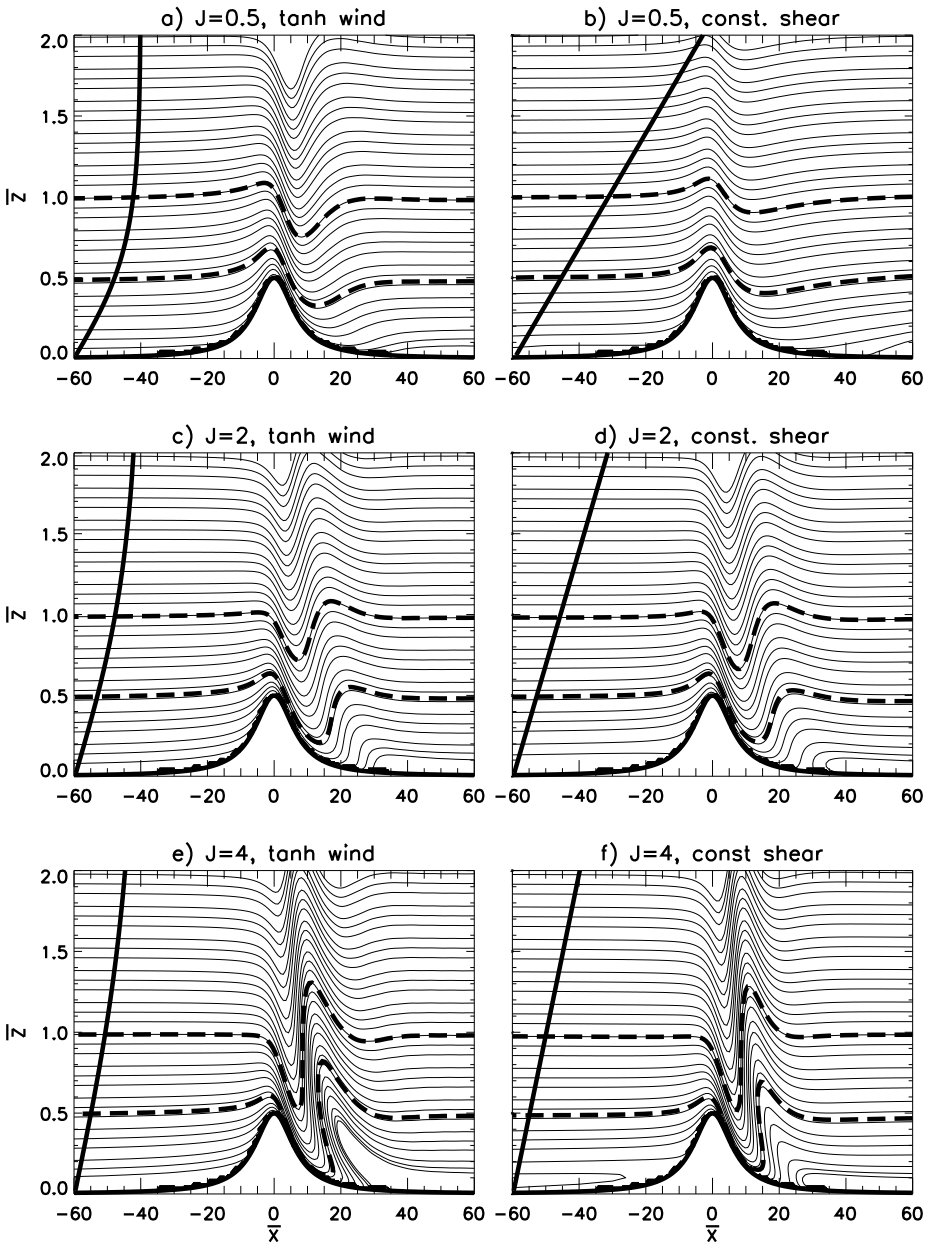

Figure 2: Isentropic surfaces predicted by the linear model when $H_N = 0.5$, $F_r = 5$ and for different value of J. Tanh incident wind and $\overline{z}_b = 0.05$: a) J=0.5, c) J=2, e) J=4. Constant shear and hydrostatic set-up in (16), $\overline{z}_b = 0.02$: b) J=0.5, d) J=2, e) J=4. In all panels the thick curve represent the incident wind U and the thick dashed curves the isentropes that initially are at the altitudes $\overline{z} = H_N$ and $\overline{z} = 2H_N$.

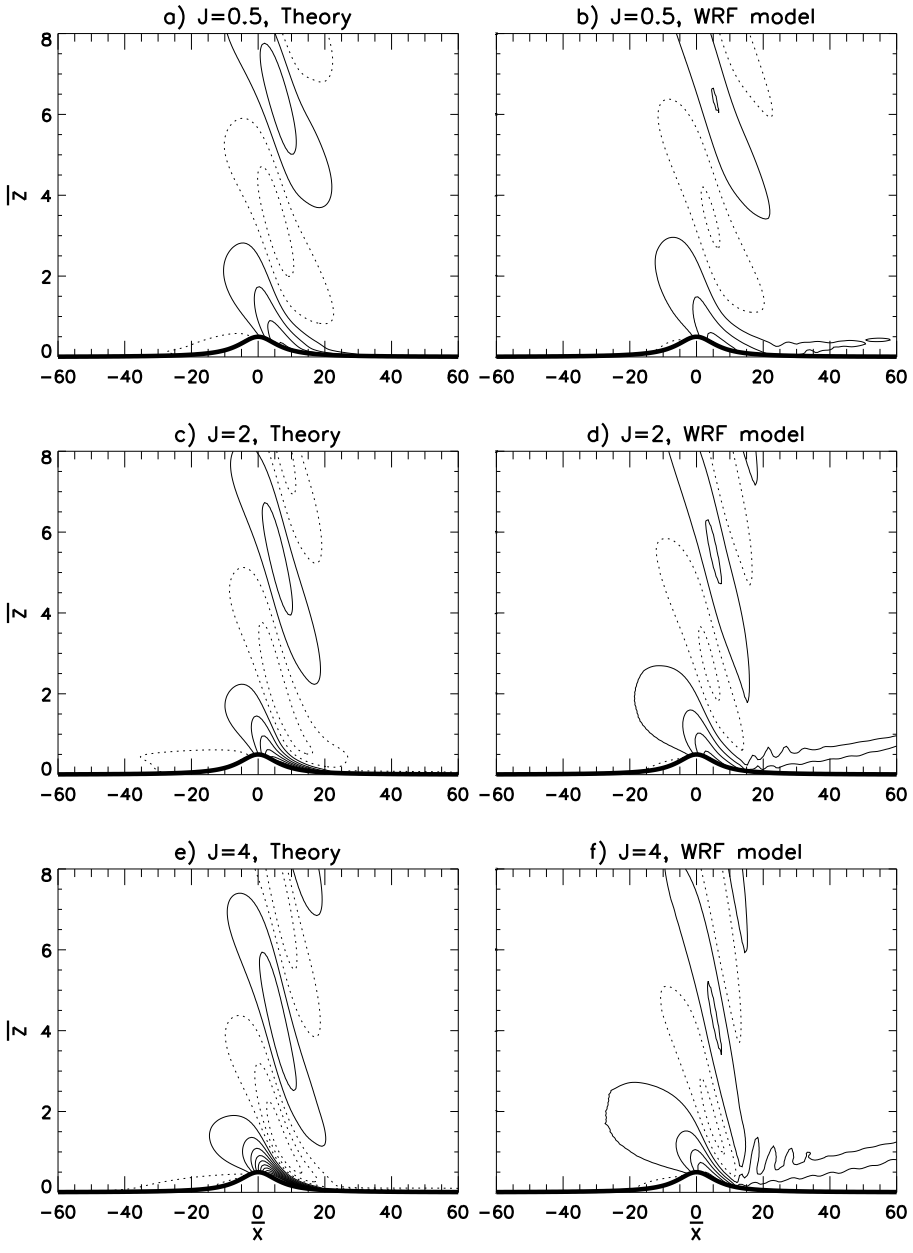

Figure 3: Non-dimensional Horizontal wind disturbances ($\overline{u}$) predicted by the theory (a, c, e) and WRF (b, d, f), for $J = 0.5$, 2, and 4, respectively. In all simulations $H_N = 0.5$ and in the linear model in (a), (c), and (e) the boundary layer scale varies as $\overline{z}_b = 0.05\sqrt{J}$. In each panel the contour interval is proportional to the background wind at the top of the hill, contours$= 0.2 * H_N/\sqrt{J}$.

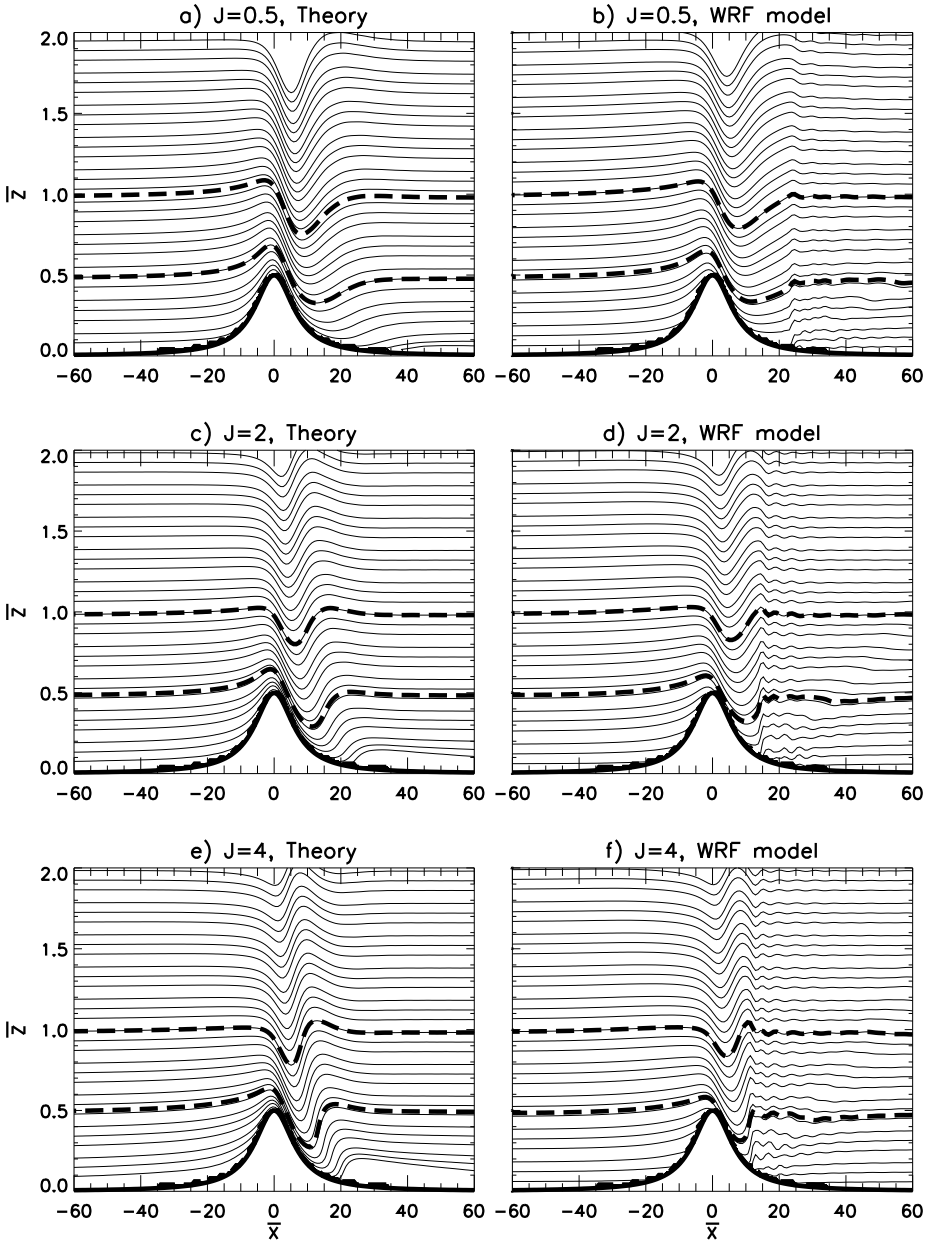

Figure 4: Isentropic surfaces predicted by the theory and WRF, same parameters as in Fig. 3

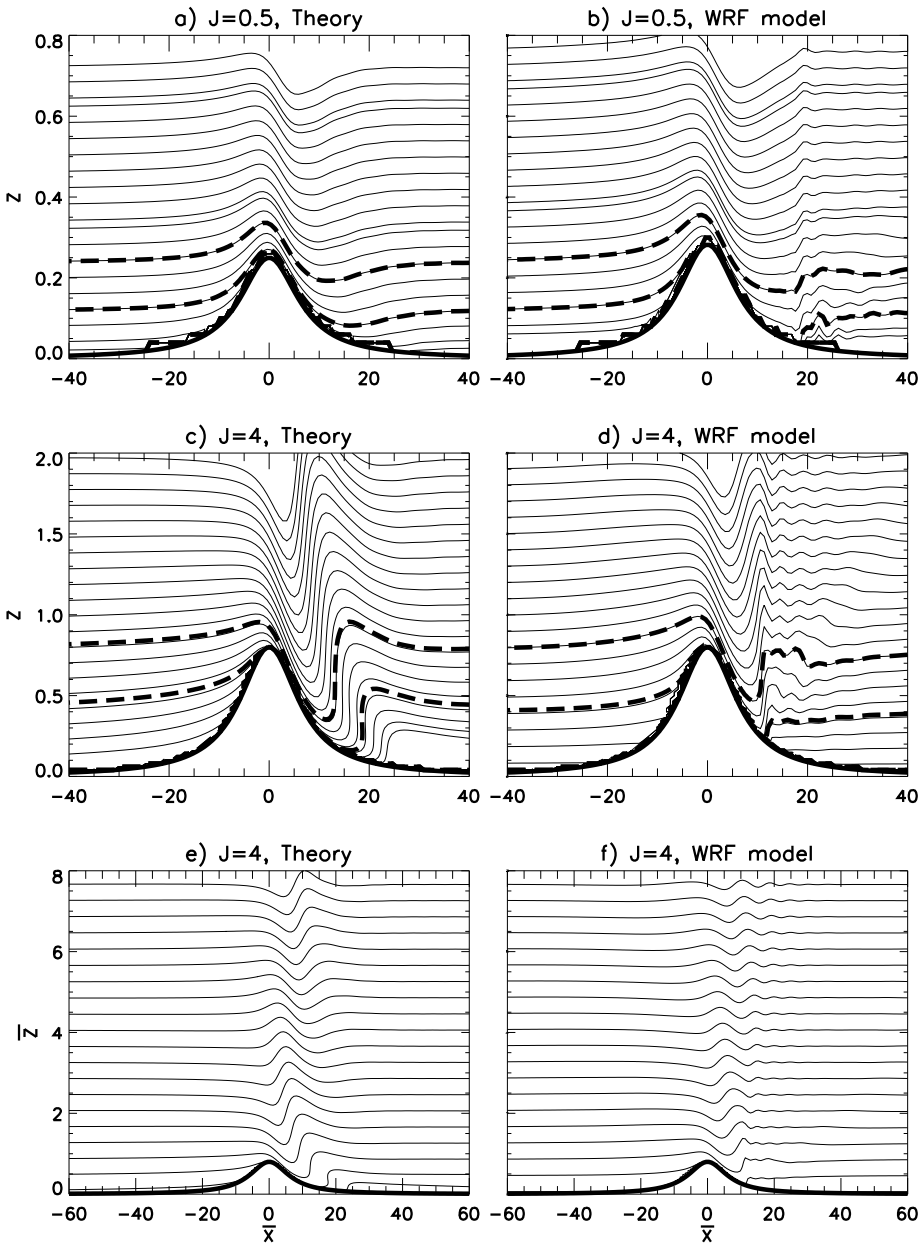

Figure 5: Same as Fig. 4 but leaving $H_N/\sqrt{J}$ =cte: a) and b) $J = 0.5$, $H_N = 0.25$; c) and d) $J = 4, H_N = 0.71$. e) and f) are enlarged views of c) and d).

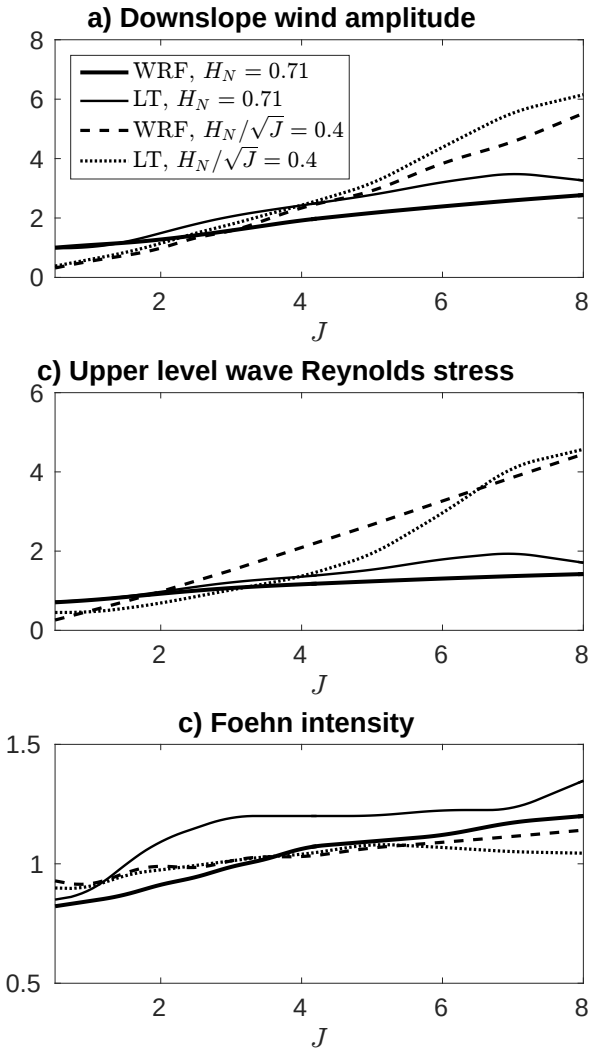

Figure 6: Global indices measuring a) the downslope wind amplitudes (24), b) the normalised wave stress (25), and c) the foehn intensity (26). The results are from 64 numerical experiments, 32 uses with WRF and 32 the "inflow linear" theory (LT). Half the simulations are done with constant height $H_N = 0.71$, the other half with constant penetration of the mountain into the shear $H_N/\sqrt{J} = 0.4$.

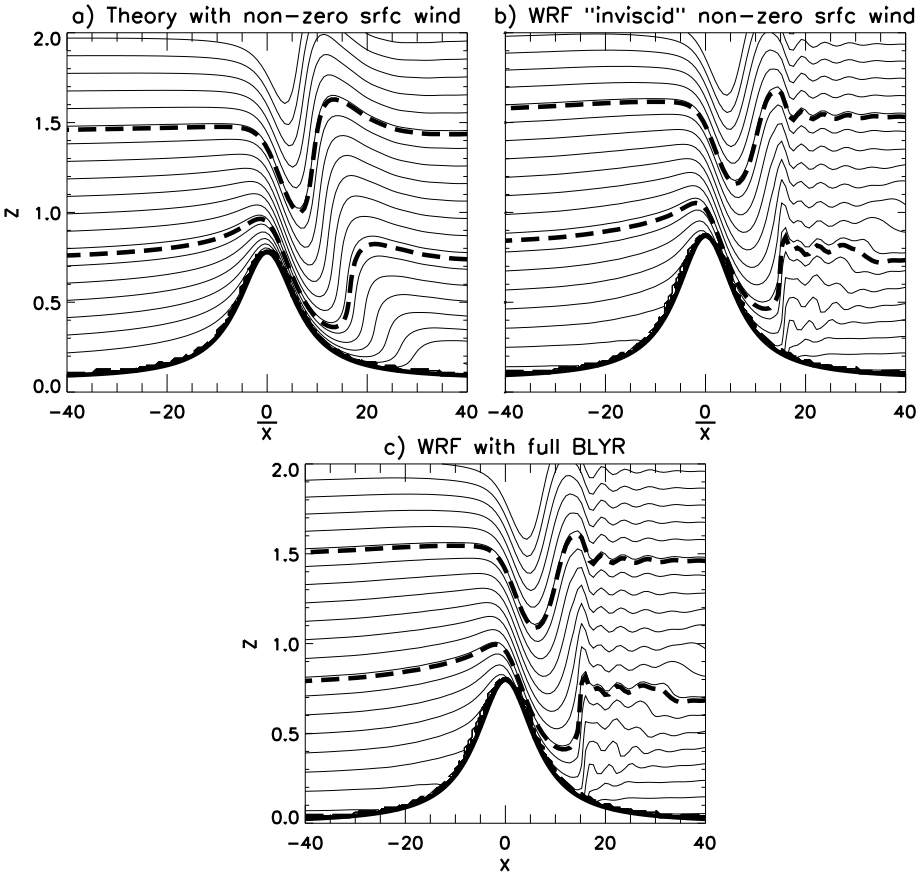

Figure 7: Sensitivity test: a) and b) are as Fig. 5c and 5d with the surface $\overline{h}$ shifted vertically by $H_N/10$. c) is as Fig. 5d but with a fully parameterized boundary layer.